AN IMPROVED NEGATIVE-MASS-INSTABILITY DISPERSION RELATION FOR HIGH-CURRENT MODIFIED BETATRONS†

BRENDAN B. GODFREY and THOMAS P. HUGHES

Mission Research Corporation, 1720 Randolph Road, S.E., Albuquerque, NM 87106

A new linearized, rigid-disk model of negative-mass instabilities in high-current betatrons is presented. The beam and accelerator cavity cross sections are taken to be rectangular so that the electromagnetic fields can be evaluated exactly in toroidal geometry. Growth rates from the model agree well with results of three-dimensional numerical simulations for beams and cavities with rectangular or circular cross sections. Generally, negative-mass-instability growth rates are greatest for beam energies within a factor of two of the so-called transition energy, and in that energy regime, they scale inversely with the square root of the toroidal magnetic field strength. At much higher energies, growth rates are nearly independent of toroidal field strength. Growth rates increase with beam current and toroidal mode number, but the scaling laws are complicated by competition between capacitive and inductive components of the toroidal cavity fields. In some instances, the negative-mass instability is supplanted by slower-growing instabilities which arise from resonant coupling between longitudinal and transverse beam modes. Certain growth rate cutoffs predicted by previous theories of the negative-mass instability are not observed either in our model or in computer simulations.

1. INTRODUCTION

Betatrons employing toroidal magnetic fields,[1,2] possibly augmented by strong-focusing fields,[3–6] hold promise for accelerating multi-kiloampere electron beams to high energies. However, beam stability is an important issue not yet completely resolved. Among instabilities, the negative-mass mode is probably the most serious, as it has been for other electron ring devices.[7] In this paper, we present a theory of the negative-mass and closely related instabilities for high-current conventional and modified[1,2] betatrons. Since the model we use results in quite elaborate expressions (despite the fact that we treat only the case of a monoenergetic beam in a smooth-walled, perfectly conducting cavity), some explanation of our reasons for developing this model seems in order. In the derivation of the well-known negative-mass instability result for long-wavelength modes on a pencil beam,[8] toroidal corrections to the fields are ignored. In addition, the approximation $\gamma_\phi = (1 - \beta_\phi^2)^{-1/2} \approx \gamma_b$ is made, where $\beta_\phi c$ is the toroidal phase velocity of the mode, and γ_b is the beam relativistic factor. If the latter approximation is not made, then the (presumably more exact) dispersion

relation predicts that when the product of the beam current times the beam energy is large enough, the instability disappears. For a fixed beam energy, this leads to the counterintuitive conclusion that the beam becomes stable as the current is increased. Furthermore, when this type of model is applied to the modified betatron,[9] the growth rates obtained are in significant disagreement with particle-in-cell computer simulations.[10]

In a previous paper,[10] we developed a model for negative-mass instabilities which included first-order toroidal corrections to the electromagnetic fields. No approximation was made for γ_ϕ. The growth rates we obtained agreed quite well with simulation results. However, growth rate cutoffs were again predicted both for the conventional and modified betatron, while no cutoffs were seen in the simulations. In addition, agreement deteriorated at large toroidal mode numbers (i.e., short wavelengths). This calculation strongly suggested to us that the discrepancies were due to inaccuracies in the treatment of the fields, rather than due to the rigid-risk model for the beam.

To reduce the discrepancies between theory and simulations, we have developed a model of negative-mass instabilities which relaxes many of the approximations in the earlier work by ourselves and others. We use a Green's function method to evaluate exactly the fields of the electron beam in the accelerator cavity for arbitrary beam and cavity dimensions and arbitrary aspect ratios. No constraints are placed on instability frequencies or toroidal mode numbers. In addition, the beam need not be centered radially in the cavity. These improvements are made possible by taking the beam and cavity to have rectangular minor cross sections. This requirement is not as limiting as it might seem at first. Three-dimensional numerical simulations indicate that beam behavior in cavities of approximately square cross section is little different from that in cavities of circular cross section, provided the cross-sectional areas are equal.

A simplified analytical dispersion relation derivable from the new model is qualitatively similar to the dispersion relation of Ref. 10. Numerical coefficients are, however, much improved, and the new model exhibits even better agreement than its predecessor with negative-mass-instability linear growth rates from numerical simulations. In particular, the discrepancies with the few simulations performed at high energies and at large toroidal mode numbers have been eliminated.[11] More importantly, the present analysis is on firmer conceptual grounds, which permits us to apply it more confidently in new regions of parameter space.

Interesting behavior is predicted by the revised model. Inductive electric fields dominate electrostatic fields at large toroidal mode numbers, giving rise to a new, slower-growing instability which supplants the negative mass there. The transition between instabilities can, to a degree, be shifted to lower toroidal modes by moving the electron beam toward the inner wall of the cavity. (The analogous but simpler case of inductive effects in a fast-rotating electron layer immersed in a strong azimuthal magnetic field is treated in Ref. 12. Besides providing a check on the betatron results, the electron layer analysis permits greater physical insight.) High-frequency electromagnetic phenomena also are encompassed by

the dispersion relation. As expected, electromagnetic effects are small in modified betatrons with moderate-size cavity cross sections. (Strong-focusing betatrons, on the other hand, are subject to virulent narrow-band three-wave electromagnetic instabilities in certain parameter regimes.)[13] No growth rate cutoffs of the type predicted by the models of Refs. 9 and 10 are seen in either the theory or the simulations.

This paper is organized as follows. In Section 2, the beam currents and equations of motion are specified in the rigid-disk approximation. The self-consistent electromagnetic fields of the perturbed beam in the toroidal accelerator cavity are then evaluated exactly using Green's functions. Although the resulting dispersion relation is algebraically very complicated, useful analytical growth rate expressions can be derived in most cases. The analysis is developed in Section 3, and Table I catalogues most of the findings. Typical numerical coefficients appearing in the analytical expressions are determined in Section 4. In Section 5, the full dispersion relation is solved numerically for 1- and 10-kA beams over a wide range of electron energies, magnetic fields, and mode numbers. Comparisons with three-dimensional simulation code data are provided. The analytical expressions, numerical growth rate curves, and simulation results generally all agree quite well. Our results are summarized and their implications discussed in Section 6.

2. DERIVATION OF THE LINEAR DISPERSION RELATION

We consider a rectangular beam in a rectangular torus with dimensions as shown in Fig. 1. In general, the beam cross section need not be the same shape as that of the torus, and the beam need not be centered radially. Axial centering is, of course, required for a static equilibrium.

As in earlier works,[9,10,13] we treat the beam as a string of rigid disks. The disks
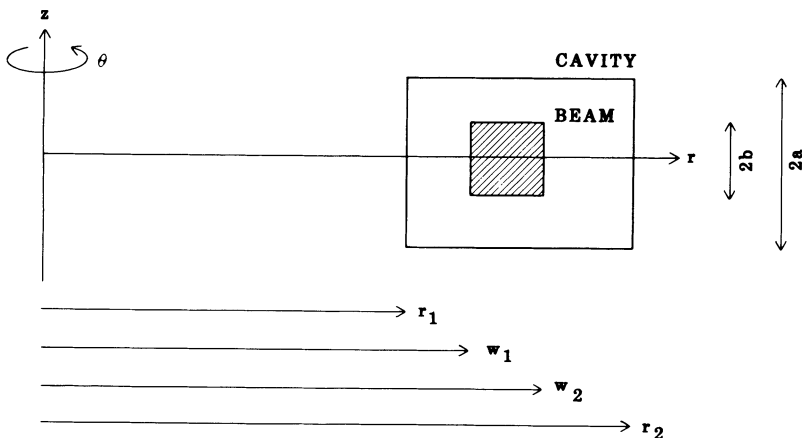

FIGURE 1   Cross section of rectangular beam in rectangular betatron cavity.

are free to move in any direction, but have no internal degrees of freedom. Thus, the internal dynamics of the beam, and temperature effects in particular, are ignored. (Instability stabilization by a spread in electron circulation frequencies has been discussed by various authors.)[8,14-16] The rigid-disk model relies on the assumption that the transverse dimensions of the beam are small compared with those of the cavity. For the modes we are concerned with, the scale length for the transverse variation of the fields is on the order of the minor radius of the cavity. Within this context, the beam centroid equations of motion are obtained by integrating the single-particle equations over the beam cross section. Thus, the beam-equilibrium radial-force balance equation is given by

$$\frac{1}{A} \int \left(E_r + \frac{V_\theta}{R} r B_z \right) dA + \gamma \frac{V_\theta^2}{R} = 0. \tag{1}$$

In arriving at Eq. (1), we have taken the beam density to be constant and, consistent with the rigid-disk approximation, the beam velocity to vary linearly with radius. R is the charge-weighted equilibrium radius, V_θ is the velocity at that location, A is the cross-sectional area of the beam, and $dA = r\, dr\, dz$:

$$R = \frac{1}{A} \int r\, dA, \qquad A = \int dA. \tag{2}$$

Note that the speed of light and the electron charge and mass are scaled out of our equations. This has the effect of measuring distance and time relative to an arbitrary scale length, and potentials relative to the electron rest energy.

The linearized equations for beam motion about its equilibrium position are obtained in a similar manner.[9,10]

$$\gamma\, \delta\ddot{z} = \frac{1}{A} \int \left(\delta E_z - \frac{V_\theta}{R} r\, \delta B_r \right) dA + B_\theta\, \delta\dot{r} + \frac{1}{A} \int \left(\frac{\partial E_z}{\partial z} - \frac{V_\theta}{R} r \frac{\partial B_r}{\partial z} \right) dA\, \delta z, \tag{3}$$

$$\gamma\, \delta\ddot{r} = \frac{1}{A} \int \left(\delta E_r + \frac{V_\theta}{R} r\, \delta B_z \right) dA - B_\theta\, \delta\dot{z} + \frac{1}{A} \int \left(\frac{\partial E_r}{\partial r} + \frac{V_\theta}{R} r \frac{\partial B_z}{\partial r} \right) dA\, \delta r$$
$$+ \left(\beta \frac{V_\theta}{R} - \gamma \frac{V_\theta^2}{R^2} \right) \delta r + \beta R\, \delta\dot{\theta}, \tag{4}$$

$$\gamma^3 R\, \delta\ddot{\theta} = -\beta\, \delta\dot{r} + \frac{1}{A} \int \frac{r}{R} \delta E_\theta\, dA, \tag{5}$$

with

$$\beta \equiv \gamma^3 \frac{V_\theta}{R} - \frac{E_r}{V_\theta}. \tag{6}$$

Perturbed quantities are preceded by a delta (e.g., δz), while unperturbed quantities are not. Total time derivatives of perturbed beam quantities are represented by dots above those quantities (e.g., $\delta\dot{z}$). B_θ is the toroidal magnetic field, averaged over the beam cross section.

Perturbed beam current and charge densities arising from these motions are

$$\delta J_z = \rho\, \delta\dot{z}, \tag{7}$$

$$\delta J_r = \rho\, \delta\dot{r}, \tag{8}$$

$$\frac{1}{r}\,\delta J_\theta = \rho\,\delta\dot\theta + \frac{V_\theta}{R}\,\delta\rho,\tag{9}$$

and

$$\delta\rho = -\frac{\partial}{\partial z}\rho\,\delta z - \frac{1}{r}\frac{\partial}{\partial r}r\,\rho\,\delta r - \frac{\partial}{\partial\theta}\rho\,\delta\theta,\tag{10}$$

where ρ is the uniform equilibrium charge density. With the exception of Eq. (9), which has been modified to take account of the beam azimuthal velocity variation with radius, these equations are taken directly from Ref. 10. It is easy to show that they satisfy the continuity equation.

For the calculations outlined below, it is convenient to express Maxwell's equations for the perturbed field quantities as a vector wave equation for the electric fields:

$$\left(\frac{\partial^2}{\partial t^2} - \nabla^2\right)\delta\mathbf{E} = -\frac{\partial}{\partial t}\delta\mathbf{J} - \nabla\,\delta\rho.\tag{11}$$

Once Eq. (11) is solved, the magnetic fields are determined simply from

$$\frac{\partial}{\partial t}\delta\mathbf{B} = -\nabla\times\delta\mathbf{E}.\tag{12}$$

The solution of Eqs. (1)–(12) is straightforward but very lengthy. It proceeds as follows. The perturbed quantities are taken to have azimuthal and temporal variations of the usual form, namely, $\exp[i(l\theta - \omega t)]$. Equation (11), together with its source terms, Eqs. (7)–(10), are then solved for the perturbed electric fields, using a vector Green's function in cylindrical coordinates.[17,18] The construction of the Green's function is described in the Appendix. Next, the perturbed magnetic fields are obtained by direct substitution in Eq. (12). The equilibrium fields are determined in a similar manner. Eliminating the various field components from Eqs. (3)–(5) then leaves a 3×3 Hermitian matrix equation in δr, $\delta\theta$, δz. Its determinant is the desired dispersion relation.

The dispersion relation, cast in the form used in our earlier work,[10] is

$$(\Omega^2 - \omega_z^2)\left(\Omega^2 - \omega_r^2 - \frac{\chi}{\Omega^2 - \varepsilon}\right) - \Omega^2\frac{B_\theta^2}{\gamma^2} = 0,\tag{13}$$

where $\Omega = \omega - l\omega_0$ and $\omega_0 = V_\theta/R$. The axial and radial oscillation frequencies are given by

$$\omega_z^2 = -n\omega_0\frac{B_z^0}{\gamma} - \frac{\rho}{\gamma A}\left\{\sum_{k,^l\lambda_E}\frac{(\rho_E^k\rho_E^\lambda)^2}{(k^2 + {}^l\lambda_E^2 - \omega^2)^l\lambda_E^2}[(k^2 - \Omega^2)^l\lambda_E^2 - (l\omega_0 k)^2]\right.$$
$$\left. -\sum_{k,^0\lambda_E}\frac{(\rho_B^k\hat\rho_E^\lambda)^2 k^2}{k^2 + {}^0\lambda_E^2} - V_\theta^2\sum_{k,^l\lambda_B}\frac{(\rho_E^k\hat\rho_B^\lambda)^2 k^2}{(k^2 + {}^l\lambda_B^2 - \omega^2)^l\lambda_B^2} + V_\theta^2\sum_{k,^0\lambda_B}\frac{(\rho_B^k\hat\rho_B^\lambda)^2 k^2}{(k^2 + {}^0\lambda_B^2)^0\lambda_B^2}\right\},\tag{14}$$

$$\omega_r^2 = n\omega_0\frac{B_z^0}{\gamma} + \omega_0^2 - \frac{\beta}{\gamma}\omega_0 + \frac{\beta^2}{\gamma^4} - \frac{\rho}{\gamma A}\left\{\sum_{k,^l\lambda_E}\frac{(\rho_B^k\hat\rho_E^\lambda)^2}{(k^2 + {}^l\lambda_E^2 - \omega^2)^l\lambda_E^2}({}^l\lambda_E^2 - \omega^2)\right.$$
$$\left. -\sum_{k,^0\lambda_E}\frac{(\rho_B^k\rho_E^\lambda)^2}{k^2 + {}^0\lambda_E^2}\alpha - \sum_{k,^l\lambda_B}\frac{[\rho_B^k(V_\theta{}^l\lambda_B\rho_B^\lambda - l\omega/R\hat\rho_B^\lambda)]^2}{(k^2 + {}^l\lambda_B^2 - \omega^2)^l\lambda_B^2} + V_\theta^2\sum_{k,^0\lambda_B}\frac{(\rho_B^k\hat\rho_B^\lambda)^2}{k^2 + {}^0\lambda_B^2}\right\},\tag{15}$$

the longitudinal oscillation frequency (squared) by

$$\varepsilon = -\frac{\rho}{\gamma^3 A}\left[\frac{l^2}{R^2}\sum_{k,{}^l\lambda_E}\frac{(\rho_B^k\rho_E^\lambda)^2}{(k^2+{}^l\lambda_E^2-\omega^2){}^l\lambda_E^2}({}^l\lambda_E^2-\omega^2)-\omega^2\sum_{k,{}^l\lambda_B}\frac{(\rho_B^k\hat{\rho}_B^\lambda)^2}{(k^2+{}^l\lambda_B^2-\omega^2){}^l\lambda_B^2}\right],$$

(16)

and the coupling coefficient by

$$\chi = \left\{\frac{\beta}{\gamma^2}\Omega+\frac{\rho}{\gamma^2 A}\left[\frac{l}{R}\sum_{k,{}^l\lambda_E}\frac{(\rho_B^k)^2\rho_E^\lambda\hat{\rho}_E^\lambda}{(k^2+{}^l\lambda_E^2-\omega^2){}^l\lambda_E^2}({}^l\lambda_E^2-\omega^2)\right.\right.$$

$$\left.\left.+\omega\sum_{k,{}^l\lambda_B}\frac{(\rho_B^k)^2\left(V_\theta{}^l\lambda_B^2\rho_B^\lambda-\frac{l}{R}\omega\tilde{\rho}_B^\lambda\right)\hat{\rho}_B^\lambda}{(k^2+{}^l\lambda_B^2-\omega^2){}^l\lambda_B^2}\right]\right\}^2-\frac{\beta^2}{\gamma^4}(\Omega^2-\varepsilon).$$

(17)

B_z^0 is the applied vertical magnetic field, and n is the betatron index. The vertical field is determined from radial-force balance, Eq. (1):

$$B_z^0 = -\beta-\frac{\rho V_\theta}{A}\sum_{k,{}^0\lambda_B}\frac{(\rho_B^k)^2\rho_B^\lambda\hat{\rho}_B^\lambda}{k^2+{}^0\lambda_B^2},$$

(18)

with, from Eq. (6),

$$\beta = \gamma^3\omega_0-\frac{\rho}{V_\theta A}\sum_{k,{}^0\lambda_E}\frac{(\rho_B^k)^2\rho_E^\lambda\hat{\rho}_E^\lambda}{k^2+{}^0\lambda_E^2}.$$

(19)

Sums in the preceding six equations are performed over the axial and radial eigenvalues of the vacuum electromagnetic fields in the toroidal cavity. The axial eigenvalues are given by

$$k = \frac{\pi}{2a}j \quad (0\le j<\infty).$$

(20)

The axial form factors ρ_E^k and ρ_B^k are obtained by integrating the corresponding eigenfunctions, sines and cosines, over the beam cross section:

$$\rho_E^k = \begin{cases} \dfrac{2b}{\sqrt{2a}} & (j=0), \\[2mm] 0 & (j\text{ odd}), \\[2mm] \dfrac{2}{\sqrt{a}}\dfrac{\sin(kb)}{k} & (j\text{ even},\, j>0), \end{cases}$$

(21)

$$\rho_B^k = \begin{cases} \dfrac{2}{\sqrt{a}}\dfrac{\sin(kb)}{k} & (j\text{ odd}), \\[2mm] 0 & (j\text{ even}). \end{cases}$$

(22)

The radial eigenvalues satisfy the usual vacuum dispersion relations:

$$J_l({}^l\lambda_E r_1)Y_l({}^l\lambda_E r_2)-J_l({}^l\lambda_E r_2)Y_l({}^l\lambda_E r_1)=0,$$

(23)

$$J_l'({}^l\lambda_B r_1)Y_l'({}^l\lambda_B r_2)-J_l'({}^l\lambda_B r_2)Y_l'({}^l\lambda_B r_1)=0.$$

(24)

For low l mode numbers, these eigenvalues can be approximated as

$$'\lambda_E \approx \begin{cases} 0 & (j = 0), \\ \dfrac{\pi}{r_2 - r_1} j & (j > 0), \end{cases} \tag{25}$$

$$'\lambda_B \approx \begin{cases} \dfrac{l}{R} & (j = 0), \\ \dfrac{\pi}{r_2 - r_1} j & (j > 0). \end{cases} \tag{26}$$

The eigenvalue $'\lambda_E(j = 0)$ is not included in the sums since the eigenfunction itself vanishes in this case. As l increases, the values of the low-lying electric and magnetic eigenvalues are pushed up.

The radial form factors are expressed as integrals over the vacuum eigenfunctions, because simpler expressions do not, in general, exist:

$$\rho_E^\lambda = \int_{w_1}^{w_2} g_E^\lambda r \, dr, \tag{27}$$

$$\hat{\rho}_E^\lambda = -'\lambda_E \int_{w_1}^{w_2} g_E^{\lambda\prime} r \, dr, \tag{28}$$

$$\rho_B^\lambda = \int_{w_1}^{w_2} g_B^\lambda \frac{r}{R} r \, dr, \tag{29}$$

$$\hat{\rho}_B^\lambda = -'\lambda_B \int_{w_1}^{w_2} g_B^{\lambda\prime} \frac{r}{R} r \, dr, \tag{30}$$

$$\tilde{\rho}_B^\lambda = \int_{w_1}^{w_2} g_B^\lambda \frac{R}{r} r \, dr, \tag{31}$$

and

$$\alpha = [g_E^\lambda - '\lambda_E r g_{E}^{\lambda\prime}]_{w_1}^{w_2} / \rho_E^\lambda. \tag{32}$$

Recall that α, which typically is of order unity, occurs only in Eq. (15). The eigenfunctions entering into Eqs. (27)–(32) are

$$g_E^\lambda = C_E^{-1/2}[J_l('\lambda_E r)Y_l('\lambda_E r_2) - J_l('\lambda_E r_2)Y_l('\lambda_E r)], \tag{33}$$

$$g_B^\lambda = C_B^{-1/2}[J_l('\lambda_B r)Y_l'('\lambda_B r_2) - J_l'('\lambda_B r_2)Y_l('\lambda_B r)]. \tag{34}$$

The quantities J_l and Y_l are standard Bessel functions of the first and second kinds. A prime indicates differentiation with respect to the argument. The normalization constants in these expressions are[19]

$$C_E = \tfrac{1}{2}[r^2(g_E^{\lambda\prime})^2]_{r_1}^{r_2}, \tag{35}$$

$$C_B = \tfrac{1}{2}\left[\left(r - \frac{l}{'\lambda_B}\right)^2 (g_B^\lambda)^2\right]_{r_1}^{r_2}. \tag{36}$$

Accurate solutions of Eqs. (13)–(36) clearly must be obtained numerically.

However, a qualitative picture of instability scaling can be developed with surprising ease.

3. APPROXIMATE INSTABILITY GROWTH RATE SCALINGS

The negative-mass and related instabilities typically occur at frequencies approximated by $\Omega \approx 0$. Thus, provided $l\omega_0$ is well below the electromagnetic cutoff for toroidal mode l of the betatron cavity, which is usually the case, we can safely replace ω by $l\omega_0$ in the denominators of the field contributions (the sums) in Eqs. (14)–(17). Making the same substitution in the numerators of the field contributions in Eqs. (14)–(16) is less accurate but still tolerable. This is not true of Eq. (17), however, due to a strong cancellation between electrostatic and inductive contributions. With these approximations, the terms occurring in the dispersion relation take the form

$$\omega_z^2 \approx n\omega_0^2 - g_1 \frac{2v}{\gamma^3 b^2}, \tag{37}$$

$$\omega_r^2 \approx (1-n)\omega_0^2 - g_2 \frac{2v}{\gamma^3 b^2}, \tag{38}$$

$$\varepsilon \approx \frac{v}{\gamma^3}\left(g_3 \frac{l^2}{R^2} - g_4\omega^2\right), \tag{39}$$

$$\chi \approx \left(\gamma\omega_0\Omega + \frac{v}{\gamma^2}\frac{l}{R^2}g_5\right)^2 - \gamma^2\omega_0^2(\Omega^2 - \varepsilon), \tag{40}$$

where v is the beam current normalized to 17 kA. For a square beam roughly centered in a square cavity, the five geometrical factors are approximately

$$g_1 \approx g_2 \approx 1, \tag{41}$$

$$g_3 \approx g_4 \approx g_5 \approx \tfrac{1}{2} + \ln\left(\frac{A_c}{A}\right), \tag{42}$$

as can be verified numerically. A_c is the cavity cross-sectional area, defined similarly to A.

Although the precise values of g_1 and g_2 are not critical, the three remaining coefficients must be determined quite accurately. Expanding Eq. (40) and dropping small terms proportional to Ω^2 and v^2 yields

$$\chi \approx 2\Omega\omega_0 \frac{l}{R^2}\frac{v}{\gamma}(g_5 - g_4 V_\theta^2) + \frac{l^2}{R^4}\frac{v}{\gamma}(g_3 - g_4 V_\theta^2). \tag{43}$$

Thus, the coupling term χ between longitudinal and transverse beam modes depends sensitively upon the differences between g_5 and g_4, and between g_3 and g_4. Numerical evaluations of these factors (see Section 4) indicate that the second term in Eq. (43) is more often the larger, in which case

$$\chi \approx \frac{\gamma^2}{R^2}\varepsilon_0, \tag{44}$$

where ε_0 is ε evaluated at $\Omega = 0$. This finding is noteworthy, because the first term in Eq. (43) gives rise to the spurious growth rate cutoffs mentioned in Section 1. Having determined that this term is negligible these cutoffs disappear [see Eqs. (50) and (56) below].

3.1. Conventional Betatron at High Energies

Let us now specialize to a high-current conventional betatron, for which the general dispersion relation is

$$(\Omega^2 - \omega_r^2)(\Omega^2 - \varepsilon) = \chi. \tag{45}$$

For an equilibrium to exist in the conventional betatron at high current, γ must be sufficiently large that the first term in Eq. (38) dominates the second. Then, Eq. (45) becomes approximately

$$\Omega^4 - \omega_r^2 \Omega^2 - \chi = 0, \tag{46}$$

with solutions

$$\Omega^2 = \frac{\omega_r^2}{2} \pm \left[\left(\frac{\omega_r^2}{2} \right)^2 + \chi \right]^{1/2}. \tag{47}$$

For small χ, i.e., weak coupling between longitudinal and transverse beam modes,

$$\frac{4\chi}{\omega_r^2} \approx \left(\frac{2l}{1-n} \right)^2 \frac{\nu}{\gamma} (g_3 - g_4 V_\theta^2) \ll 1, \tag{48}$$

the two pairs of roots in Eq. (47) reduce to

$$\Omega^2 \approx \omega_r^2, \quad -\chi/\omega_r^2. \tag{49}$$

The former represents transverse (in r) oscillations, which are stable, and the latter represents predominantly longitudinal oscillations, one of which is unstable, with a growth rate

$$\Gamma = \frac{l}{R} \left[\frac{1}{1-n} \frac{\nu}{\gamma} (g_3 - g_4 V_\theta^2) \right]^{1/2} \tag{50}$$

if χ (equivalently, ε_0) is positive. Equation (50) becomes the usual negative-mass-instability growth rate expression when $g_3 = g_4$.[8,20] However, the instability vanishes if χ is negative. This stabilization of the negative-mass effect is caused by inductive coupling of the beam to the accelerator cavity,[21,22] which is discussed further in the next section.

With increasing l, the inequality of Eq. (48) is eventually reversed, giving rise to strong coupling between the longitudinal and transverse modes. One unstable hybrid mode with a growth rate given by

$$\Gamma = \frac{l^{1/2}}{R} \left[\frac{\nu}{\gamma} (g_3 - g_4 V_\theta^2) \right]^{1/4} \tag{51}$$

occurs if χ is positive, and two unstable modes with growth rates smaller by a factor of $1/\sqrt{2}$ occur otherwise. Numerical calculations performed to date suggest that the latter possibility is much more common. Note that the growth rate at large l, Eq. (51), scales as $l^{1/2}$, in contrast to the growth rate at small l, Eq. (50), which scales as l.

Instabilities in a modified betatron can be evaluated in a manner similar to that used for the conventional betatron, provided the poloidal cyclotron frequency B_θ/γ significantly exceeds the toroidal cyclotron frequency ω_0. We distinguish between beam energies comparable to and much greater than the transition energy γ_{tr}, defined as the energy at which ω_z vanishes. Since the former regime has no counterpart in the conventional betatron, we consider it later.

3.2. Modified Betatron at High Energies

For the modified betatron at high energies, Eq. (13) reduces to

$$\Omega^4 - \Omega^2(\omega_B^2 + \varepsilon_0) - \frac{\omega_z^2\chi}{B_\theta^2/\gamma^2} = 0, \tag{52}$$

where

$$\omega_B^2 = \frac{\omega_r^2\omega_z^2}{B_\theta^2/\gamma^2} \tag{53}$$

is the poloidal drift frequency. (In obtaining these expressions we have assumed also that $\varepsilon \ll \omega_0^2$, which is true in most cases of interest.) Solutions to Eq. (52) are

$$\Omega^2 \approx \frac{\omega_B^2 + \varepsilon_0}{2} \pm \left[\left(\frac{\omega_B^2 + \varepsilon_0}{2}\right)^2 + \frac{\omega_z^2\chi}{B_\theta^2/\gamma^2}\right]^{1/2}. \tag{54}$$

As before, we consider the limits of small and large χ. For small χ, Eq. (54) reduces to

$$\Omega^2 \approx \omega_B^2 + \varepsilon_0, \quad -\frac{\omega_z^2\chi}{B_\theta^2/\gamma^2}\bigg/(\omega_B^2 + \varepsilon_0). \tag{55}$$

When $\omega_B^2 \gg \varepsilon_0$, Eq. (55) in turn becomes

$$\Omega^2 \approx \omega_B^2, \quad -\chi/\omega_r^2. \tag{56}$$

Note that the second root in Eq. (56) is identical to that in Eq. (49). Consequently, the toroidal magnetic field has no effect on the negative-mass instability whenever

$$B_\theta^2 v \frac{l^2}{R^2} \ll \frac{\gamma^5\omega_z^2\omega_r^2}{g_3 - g_4 V_\theta^2}. \tag{57}$$

Very large currents and applied fields are needed to violate this inequality, except at small γ.

In the opposite limit, $\omega_B^2 \ll \varepsilon_0$, Eq. (55) simplifies to

$$\Omega^2 \approx \varepsilon_0, \quad \frac{-\omega_z^2\chi/\varepsilon_0}{B_\theta^2/\gamma^2}. \tag{58}$$

TABLE I

Approximate Solutions to the Dispersion Relation, Eq. (13), for Conventional Betatrons and for Modified Betatrons Well Above the Transition Energy. Solutions are Categorized by the Toroidal Field Strength B_θ and the Coupling Coefficient χ.

B_θ	χ	Ω^2	Case
$\omega_B^2 \gg \omega_0^2$	$\|\chi\| \ll \left(\dfrac{\omega_r^2}{2}\right)^2$	$\omega_r^2, \ -\dfrac{\chi}{\omega_r^2}$	1A
	$\|\chi\| \gg \left(\dfrac{\omega_r^2}{2}\right)^2$	$\pm\chi^{1/2}$	2A
$\omega_0^2 \gg \omega_B^2 \gg \varepsilon$	$\|\chi\| \ll \left(\dfrac{\omega_r\omega_B}{2}\right)^2$	$\omega_B^2, \ -\dfrac{\chi}{\omega_r^2}$	1B
	$\|\chi\| \gg \left(\dfrac{\omega_r\omega_B}{2}\right)^2$	$\pm\left(\chi\dfrac{\omega_B^2}{\omega_r^2}\right)^{1/2}$	2B
$\varepsilon \gg \omega_B^2$	$\|\chi\| \ll \left(\dfrac{\varepsilon\ \omega_r}{2\ \omega_B}\right)^2$	$\varepsilon, \ -\dfrac{\chi\ \omega_B^2}{\varepsilon\ \omega_r^2}$	1C
	$\|\chi\| \gg \left(\dfrac{\varepsilon\ \omega_r}{2\ \omega_B}\right)^2$	$\pm\left(\chi\dfrac{\omega_B^2}{\omega_r^2}\right)^{1/2}$	2C

The second of these roots can be simplified by means of Eq. (44) to the usual negative-mass-instability growth rate expression for very large toroidal fields,[23]

$$\Gamma \approx (1-n)^{-1/2}\gamma\omega_B, \tag{59}$$

which is independent of both l and v. The first root in Eq. (58) is purely longitudinal. Instability results for $\varepsilon_0 < 0$, i.e., for inductive electric fields dominating electrostatic.[12]

Returning to Eq. (54), we find that the large χ limit corresponds to a strong coupling between longitudinal and transverse modes, just as in the conventional betatron. The growth rate here is simply that described by Eq. (51), reduced by a factor of order $(B_z/B_\theta)^{1/2}$:

$$\Gamma \approx \left(\frac{\omega_z}{B_\theta/\gamma}\right)^{1/2} \frac{l^{1/2}}{R}\left[\frac{v}{\gamma}(g_3 - g_4 V_\theta^2)\right]^{1/4}. \tag{60}$$

The various cases we have considered thus far for both the conventional and the modified betatron are categorized in Table I according to the magnitudes of ω_B and χ.

3.3. Modified Betatron at Low Energies

It is more difficult to obtain useful instability growth rate estimates for the modified betatron at low beam energies, because the ordering of most terms in the dispersion relation is not uniform. Replacing ε by ε_0 often is particularly

dubious. Nonetheless, some progress can be made for ω_z^2 near zero, provided ω_r^2 is also small there. In this case, the dispersion relation reduces approximately to

$$\Omega^4 - \Omega^2 \varepsilon \left(1 - \frac{\chi/\varepsilon}{B_\theta^2/\gamma^2}\right) - \frac{\chi\omega_z^2}{B_\theta^2/\gamma^2} = 0, \tag{61}$$

which has as a formal solution

$$\Omega^2 \approx \frac{\varepsilon}{2}\left(1 - \frac{\chi/\varepsilon}{B_\theta^2/\gamma^2}\right) \pm \left[\left(\frac{\varepsilon}{2}\right)^2\left(1 - \frac{\chi/\varepsilon}{B_\theta^2/\gamma^2}\right)^2 + \frac{\chi\omega_z^2}{B_\theta^2/\gamma^2}\right]^{1/2}. \tag{62}$$

As ω_z^2 goes to zero, so does one root of Eq. (62), and replacing ε by ε_0 becomes permissible:

$$\Omega^2 \approx -\frac{\gamma^2\omega_0^2\omega_z^2}{B_\theta^2/\gamma^2}\bigg/\left(1 - \frac{\gamma^2\omega_0^2}{B_\theta^2/\gamma^2}\right). \tag{63}$$

Equation (63) is similar to the strong magnetic field expression, Eq. (58), but with a correction term in the denominator. When the denominator is positive, Eq. (63) predicts instability above the transition energy ($\omega_z^2 > 0$) and stability below. Note, however, that further below the transition energy the second term in the square root in Eq. (62) may dominate the first, i.e.,

$$-\frac{\chi\omega_z^2}{B_\theta^2/\gamma^2} > \left(\frac{\varepsilon}{2}\right)^2\left(1 - \frac{\chi/\varepsilon}{B_\theta^2/\gamma^2}\right)^2, \tag{64}$$

causing the two unstable modes often found numerically at low energies.[9,10,15] A large enough magnetic field eliminates the instability there. The approximate criterion is

$$B_\theta \gg \gamma_{tr}^2\omega_0. \tag{65}$$

Incidentally, when the toroidal magnetic field is so small that the denominator of Eq. (63) becomes negative, the root described by Eq. (63) is stable above the transition energy but unstable below. The other root in Eq. (62) is unstable throughout.

4. NUMERICAL EVALUATION OF GEOMETRICAL FACTORS

The approximate growth rate expressions obtained in the previous section all involve the geometrical factors g_1 through g_5 introduced in Eqs. (37)–(40). Solutions to the exact dispersion relation, which we will examine in the next section, exhibit some features which can be attributed to subtle changes in the relative magnitudes of these factors as certain parameters are varied. In this section, we examine these features in some detail.

Accurate calculation of the g's involves numerical evaluation of the sums in Eqs. (14)–(17). Typically, the first 20 to 40 radial and axial eigenmodes are kept in the calculations. For the sums used to evaluate ω_z^2, ω_r^2, good accuracy is achieved only when the numbers of axial and radial eigenvalues used are

approximate integer multiples of twice the cavity-to-beam ratios of the axial and radial cross-sectional dimensions, respectively.

For our present purpose, we simplify the sums in Eqs. (14)–(17) by eliminating ω, replacing it by l/R in the denominators and by $l\omega_0$ in the numerators of the terms in the sums. (These approximations are not made when we obtain solutions to the exact dispersion relation in Section 5.) The resulting expressions for g_3, g_4, and g_5 are approximately independent of beam energy, and the energy dependence of g_1 and g_2 can be made explicit as

$$g_1 = \gamma^2(g_1^a - g_1^b V_\theta^2), \tag{66}$$

$$g_2 = \gamma^2(g_2^a - g_2^b V_\theta^2). \tag{67}$$

Note that in deriving Eq. (67) we have dropped an extremely small term proportional to E_r^2, because it is inconsistent with the scaling shown.

Table III lists geometrical factors for a range of l values, based on the configuration in Table II. Their magnitudes are approximately as expected, namely, unity in the first four columns and $1/2 + \ln(A_c/A) \approx 3.72$ [see Eq. (42)] in the last three columns. More importantly, relative differences among related factors are small. The few percent difference between g_1^a and g_1^b, for instance, indicates that g_1 is essentially independent of γ for $\gamma < 10$. At much higher energies, g_1 increases as γ^2, but at such energies, self-fields have no effect on ω_z^2. Likewise, the small differences between g_5 and g_4 justifies our earlier approximation that the term in Eq. (43) linear in Ω usually can be ignored. We note here again that this has the important consequence of eliminating spurious growth rate cutoffs predicted by previous theories [see Eq. (50)].

Differences between g_3 and g_4, on the other hand, have a strong impact on the beam stability, because they can affect the magnitude and even the sign of ε and χ. At small l, g_3 slightly exceeds g_4 and as a consequence, negative-mass growth rates fall off at high energies as $\gamma^{-1/2}$ rather than the usually cited $\gamma^{-3/2}$. The difference between the two geometry factors decreases with increasing toroidal mode number, so that at $l = 11$ they are equal. At higher l, g_4 exceeds g_3, stabilizing the beam at sufficiently large energies. As we shall soon see, this

TABLE II

Typical Betatron Parameters Used in Numerical Solutions of the Dispersion Relation, Eq. (13).

Beam current	1, 10 kA
Beam energy	1–30 MeV
Toroidal magnetic field	0, 1, 10, 100 kG
Index, n	0.5
Beam inner radius, w_1	98.24 cm
Beam outer radius, w_2	101.76 cm
Beam axial half-width, b	1.76 cm
Torus inner radius, r_1	91.2 cm
Torus outer radius, r_2	108.8 cm
Torus axial half-width, a	8.8 cm

TABLE III

Approximate Geometrical Factors Computed for the Parameters in
Table II at Various Toroidal Mode Numbers

l	g_1^a	g_2^b	g_2^a	g_2^b	g_3	g_4	g_5
1	1.094	1.090	1.094	1.093	3.593	3.589	3.571
5	1.094	1.090	1.095	1.093	3.593	3.590	3.570
10	1.095	1.090	1.097	1.091	3.593	3.592	3.568
15	1.095	1.089	1.100	1.089	3.592	3.596	3.567
20	1.096	1.088	1.103	1.084	3.591	3.602	3.572
25	1.097	1.086	1.104	1.075	3.591	3.610	3.589
30	1.098	1.084	1.104	1.062	3.591	3.622	3.627
35	1.098	1.080	1.098	1.041	3.593	3.637	3.700
40	1.097	1.075	1.086	1.009	3.596	3.658	3.828

reprieve from the negative-mass instability is short-lived. For still larger l, the beam encounters the large χ regime indicated by the second, fourth, and sixth cases in Table I, and the hybrid instability discussed in the preceding section occurs.

The coefficients g_3 and g_4 represent the electrostatic and inductive electric self-field contributions to the beam longitudinal dielectric function. Electrostatic forces always exceed inductive in a straight drift tube, if no slow-wave structure is present. Evidently, the larger inductive field in a betatron is due to curvature of the beam and cavity. Ordinarily, one would expect a dominant inductive field to cause unstable longitudinal bunching, as in a Cherenkov maser.[24] The reverse, however, is true of a beam particle with effectively negative mass, for which excess electrostatic fields cause instability. To corroborate this picture, we have compared the stability of beams in betatrons to that of rotating electron layers, a simpler problem.[12] Both were immersed in very strong azimuthal guide fields to suppress negative-mass effects. Inductive fields were found to dominate electrostatic in both cases at high l values.

Table IV illustrates the changes in the geometrical coefficients for $l = 1$ as the position of the beam centroid is varied. When the beam is near either the inner or the outer wall of the cavity, g_1 is much reduced due to shorting of the axial self-field restoring forces, and g_2 is correspondingly increased. Hence, beam stability at

TABLE IV

Approximate $l = 1$ Geometrical Factors Computed for the Parameters in
Table II but with the Beam Offset Radially by Various Amounts

R (cm)	g_1^a	g_1^b	g_2^a	g_2^b	g_3	g_4	g_5
107	0.136	0.134	12.768	13.282	1.590	1.579	1.326
103	0.851	0.847	1.796	1.875	3.372	3.366	3.357
100	1.094	1.090	1.094	1.093	3.593	3.589	3.571
97	0.905	0.903	1.901	1.810	3.373	3.371	3.314
95.67	0.684	0.684	3.133	2.962	3.081	3.081	2.986
93	0.158	0.159	14.601	13.936	1.600	1.610	1.260

low energies can be affected strongly by the centering of the beam. In addition, g_4 grows relative to g_3 as R is decreased. The two become equal at $R = 95.67$ cm, and for smaller radii, the inductive field dominates. This suggests that improved stability at low l can be achieved for a high-energy beam by placing it near the inner wall of the torus.

5. NUMERICAL SOLUTION OF DISPERSION RELATION

A computer program was written to calculate the roots of the exact dispersion relation, Eq. (13), using Muller's method.[25] Typically, five seconds of CDC-7600 computer time is necessary to initialize a given set of parameters, after which roots can be obtained at a rate of about one per second.

Calculations were, for the most part, performed using the equilibrium parameters listed in Table II and for toroidal mode numbers in the range 1–30. The parameters were chosen to bracket those of the modified betatron under development at the Naval Research Laboratory.[26]

Figures 2–5 depict $l = 1, 10, 20,$ and 30 negative-mass-instability growth rates for 10-kA and 1-kA beams in 1-kG guide fields, determined directly from Eq. (13). (To convert to units of sec^{-1}, multiply growth rates by 3×10^{10}.) Results for $l = 1$ and 10 with $\gamma > 10$ agree well with Eq. (50). The growth rate scales linearly with l and $\sqrt{v}$. As predicted in Section 4, the growth rates at high energies vary roughly as $\gamma^{-1/2}$ for $l = 1$ and as $\gamma^{-3/2}$ for $l = 10$. Scaling of growth rates at low energies is not so clean, but appears to go as $(l\sqrt{v})^{1/2}$. Although the two unstable modes below γ_{tr} appear to join directly onto the one unstable mode above γ_{tr}, a closer examination indicates that a tiny gap exists, consistent with the discussion accompanying Eq. (63).

When $l > 11$ the standard negative-mass instability is cut off by inductive effects for χ negative, i.e., [see Eq. (43)] for γ greater than

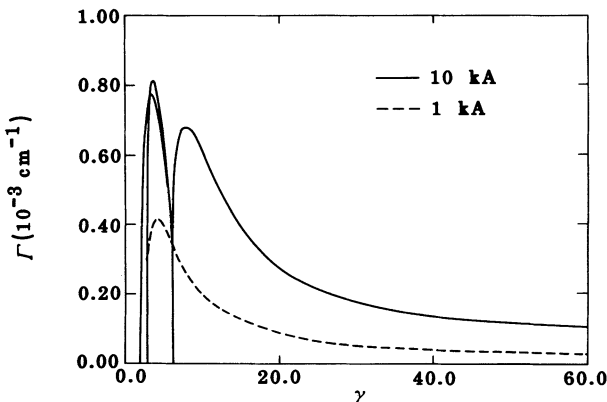$$\gamma_{co} \approx (1 - g_3/g_4)^{-1/2}. \tag{68}$$

FIGURE 2   Growth rates of the $l = 1$ negative-mass instability versus energy for 10-kA and 1-kA beams in 1-kG guide field.
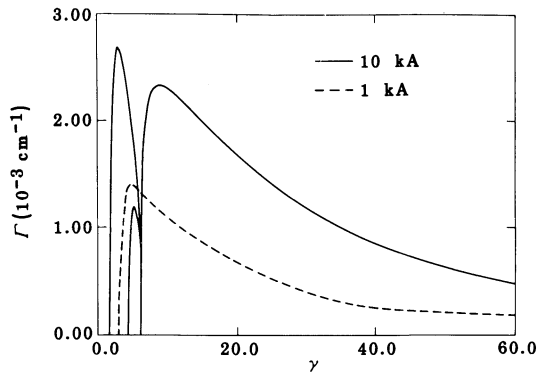
FIGURE 3 Growth rates of the $l = 10$ negative-mass instability versus energy for 10-kA and 1-kA beams in 1-kG guide field.
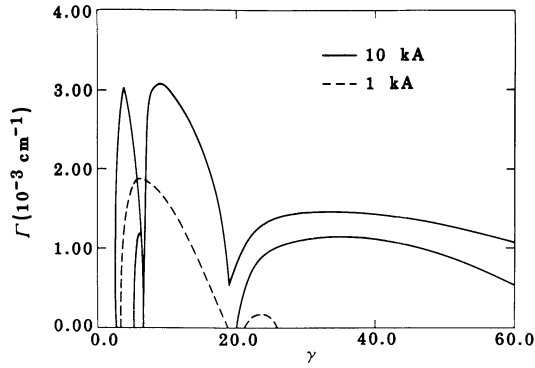

FIGURE 4 Growth rates of the $l = 20$ negative-mass instability versus energy for 10-kA and 1-kA beams in 1-kG guide field.
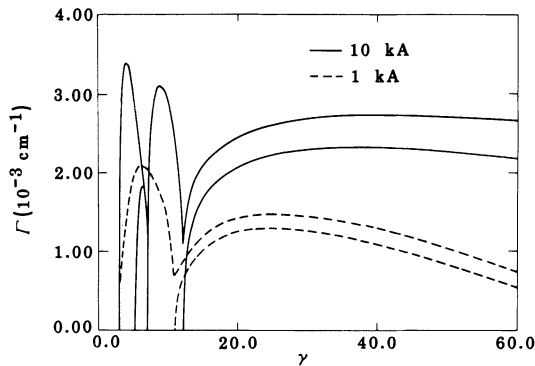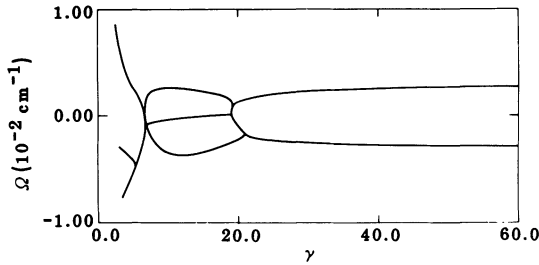

FIGURE 5 Growth rates of the $l = 30$ negative-mass instability versus energy for 10-kA and 1-kA beams in 1-kG guide field.

FIGURE 6   Doppler-shifted frequencies Ω of the modes associated with the $l = 20$ negative-mass instability of a 10-kA beam in a 1-kG guide field (see Fig. 4).

The cutoff shown for the 1-kA beam at $l = 20$ in Fig. 4 satisfies Eq. (68) well. Note also the first appearance of the hybrid negative-mass instability in a narrow band around $\gamma = 24$. The hybrid mode is much stronger in the 10-kA beam and merges directly into the usual branch of the instability at γ_{co}. The growth rates are described accurately by Eq. (54), but not yet by Eq. (60), because χ is not sufficiently large. In Fig. 5 for $l = 30$, $\gamma_{co} \approx 12$; the hybrid negative-mass instability is well-developed for both 10 kA and 1 kA.

Figure 6 illustrates the mode couplings that give rise to the different instabilities. It presents the Doppler-shifted real frequencies Ω corresponding to the growth rates of the 10-kA beam in Fig. 4. Below γ_{tr} and above γ_{co}, the longitudinal and transverse modes are strongly coupled, and two unstable branches with comparable growth rates typically exist. The standard negative-mass instability occurs within the intervening energy range, resulting from a nonresonant distortion of the longitudinal modes by curvature effects.

Instability growth rate scaling with B_θ is depicted in Figs. 7 and 8 for the 10-kA beam at $l = 1$ and 20. Results for 1-kG, 10-kG, and 100-kG guide fields are shown. Corresponding data for the conventional betatron are not given for $l = 1$, or for $l = 20$ below γ_{co}, because they are indistinguishable from the 1-kG results
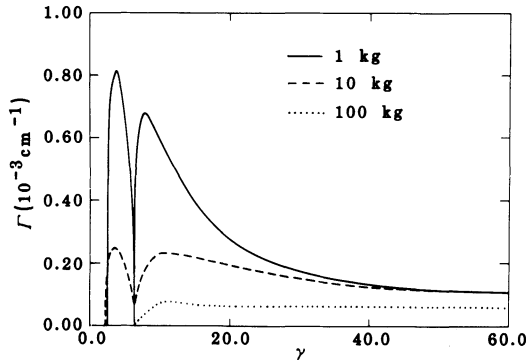

FIGURE 7   Growth rates of the $l = 1$ negative-mass instability versus energy for 10-kA beams in 1-kG, 10-kG, and 100-kG guide fields.
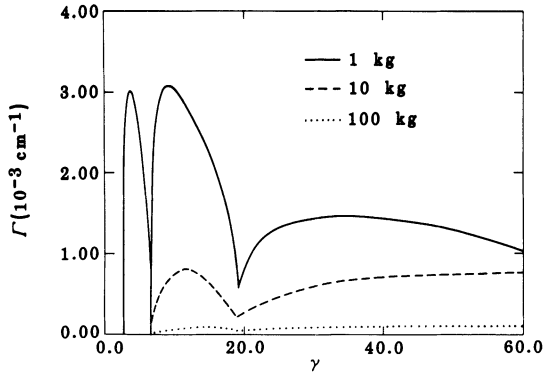
FIGURE 8   Growth rates of the $l = 20$ negative-mass instability versus energy for 10-kA beams in 1-kG, 10 kG, and 100 kG guide fields.

at energies for which an equilibrium exists (above about 9 MeV). The conventional betatron is stable above γ_{co} for $l = 20$, because the inequality of Eq. (48) is not yet strongly reversed. In general, we expect the guide field to have negligible influence on beam stability for low l (e.g., Fig. 7) so long as Eq. (57) is satisfied. For the present parameters, this is true for B_θ less than a few kG at $\gamma = 10$, and for B_θ less than a few thousand kilogauss at $\gamma = 50$. Hence, we see a steady drop in the peak of the growth rate curve as B_θ is increased above 1 kG until it obeys Eq. (59) at 100 kG. Note that growth below γ_{tr} also is eliminated. In contrast, growth rates at the highest energies shown in the plot are little reduced.

Below γ_{co}, instability behavior at $l = 20$, displayed in Fig. 8, is qualitatively similar to that at $l = 1$. Growth rates above the inductive transition energy are expected, based on Table I, to fall off with magnetic fields as $B_\theta^{-1/2}$ once B_θ somewhat exceeds ω_0. This happens above a few kilogauss for energies of interest in Fig. 8. At very high guide fields, of several thousand kilogauss, the negative-mass instability is eliminated, leaving the inductive instability mentioned in Section 4. Figure 9 gives the growth rate at infinite field strength, for which Eq.
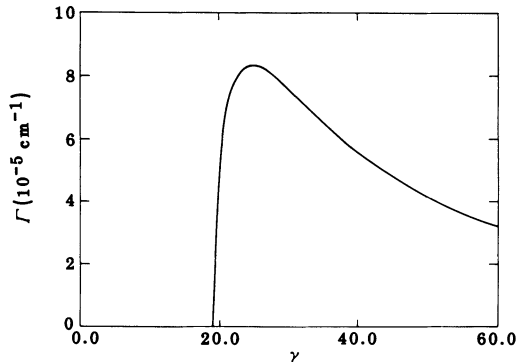

FIGURE 9   Growth rates of the $l = 20$ negative-mass instability versus energy for a 10-kA beam in an infinite guide field.

(13) collapses to

$$\Omega^2 = \varepsilon. \tag{69}$$

The instability sets in abruptly at γ_{co}. Growth scales as l/R and, for high energies, $(\nu/\gamma^3)^{1/2}$. As a test of our work, we also solved the magnetized e-layer dispersion relation in Ref. 12 with $k = \pi/b$ and obtained remarkably similar curves.

Parameters differing from those in Table II were run in a few instances. A 10-kA beam in a 1-kG guide field at $l = 1$ and 20 was considered. Changing the vertical field index n from 0.5 to 0.25 or 0.75 modified the overall magnitudes of growth rates by no more than 20%, although details were somewhat different at low energies. Likewise, increasing or decreasing the beam dimensions by a factor of two caused no differences not accountable for in terms of a rescaling of g_3, g_4, and g_5. Small changes in R also had negligible effects. Moving the beam all the way to the inner wall, on the other hand, eliminated all $l = 1$ instabilities above $\gamma = 34$ but increased growth rates by a factor of 2.5 at low energies. Growth rates at $l = 20$ were approximately doubled.

We conclude this section with a brief comparison of dispersion relation curves with growth rates determined by the three-dimensional particle-in-cell computer simulation code IVORY.[27] (IVORY decomposes the electromagnetic fields azimuthally into sines and cosines, any set of which can be followed. In this way, the development of selected toroidal modes can be treated individually, if desired.)[10] Some simulations were reported previously in Refs. 10 and 11. Figure 10 gives $l = 1$ results for a 10-kA beam in a 1-kG guide field. Agreement is excellent except for the $\gamma = 4$ data point. The discrepancy is probably due to differences in the beam radius between the theory and simulations, which shifts the location of γ_{tr}.

Figure 11 displays the simulation results for $l = 20$. Data points follow the
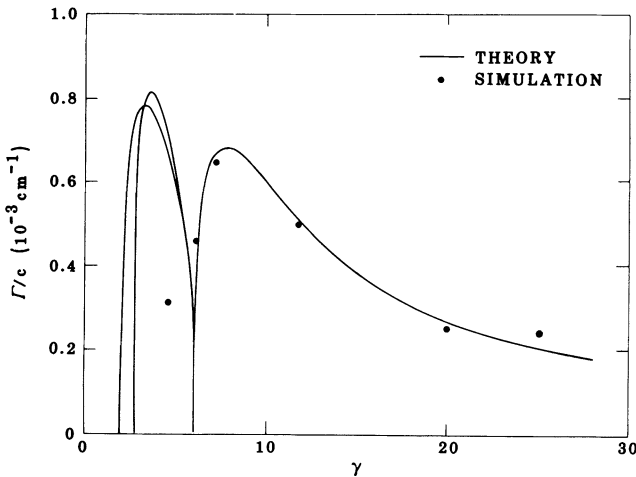

FIGURE 10   Negative-mass $l = 1$ growth rates for a 10-kA beam in a 1-kG guide field, determined from IVORY simulations, compared with dispersion relation results.
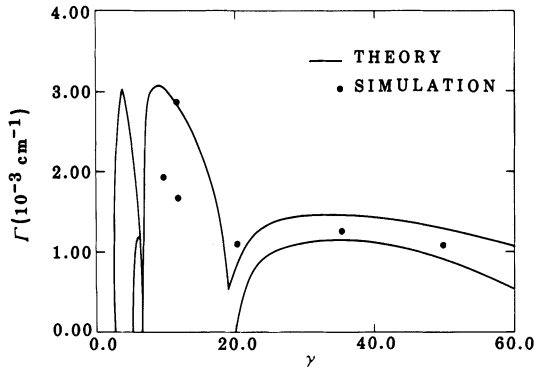
FIGURE 11   Negative-mass and hybrid instability $l = 20$ for a 10-kA beam in a 1-kG guide field, determined from IVORY simulations, compared with dispersion relation results.

theoretical curve quite well, even through the transition between the two instabilities. Note, however, that simulation results can be very sensitive to a spread in particle circulation frequencies at high l values.[15] At $\gamma = 12$, for example, a simulation using a beam equilibrium with negligible frequency spread agrees well with the rigid-disk model. By increasing the beam minor radius from 1.6 cm to 2.2 cm, thereby significantly increasing the frequency spread,[16] the instability growth rate was reduced by some 40%. Both data points are shown in the plot, as is a $\gamma = 10$ point for which significant damping effects also were evident. It is interesting that the three hybrid instability simulations (the three high-energy data points in Fig. 11) saturated benignly. Figure 12 shows the final state of the $\gamma = 50$ simulation, in which the beam has expanded about 75% in
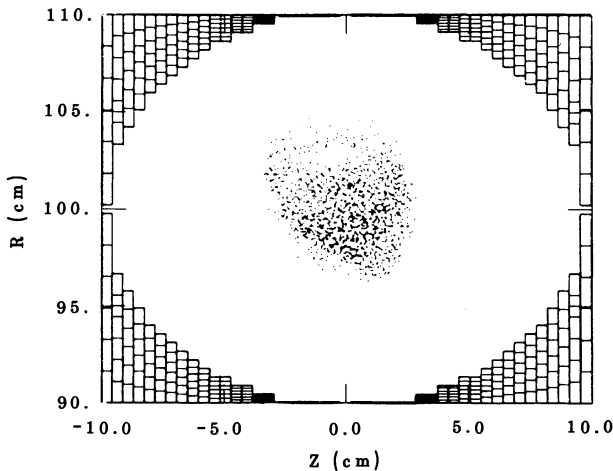

FIGURE 12   Cross section of a 10-kA, 25-MeV beam in a 1-kG guide field after saturation of the $l = 20$ hybrid instability.
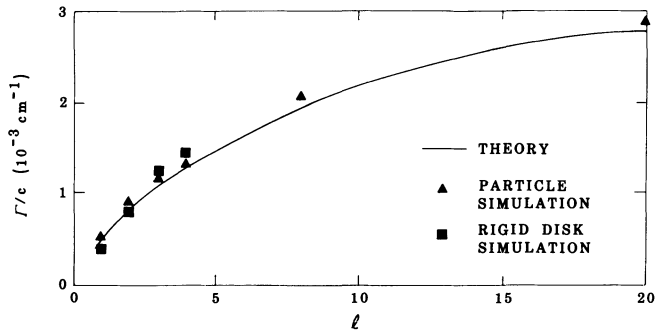
FIGURE 13 Negative-mass growth rates at various l values for a 10-kA beam in a 1-kG guide field, determined from IVORY simulations, compared with dispersion relation results. Some simulations employed rigid disks instead of discrete particles.

radius but is otherwise not significantly distorted. In contrast, all negative-mass-instability simulations to date have ended in substantial current loss to the accelerator cavity wall. See, for example, Fig. 3 of Ref. 10. This difference is probably due to the lower growth rates of the hybrid modes, although differences in the linear mode structure may also be involved. Regarding the latter, it appears from the simulations that, at the lower energies where negative-mass instability occurs, the magnetic field inhibits the radial spreading of the beam required to saturate the instability.

Figure 13 treats the same beam parameters as Figs. 10–12 but with γ held fixed at 12 and l varied from 1 to 20. Again, agreement between theory and simulation is excellent. The few simulations performed with rigid disks instead of discrete particles further vindicate the rigid-disk approximation made in our model.

6. SUMMARY AND DISCUSSION

We have developed an improved rigid-disk model for high-current, low-temperature beams in conventional and modified betatrons. The resulting dispersion relation, although quite complicated, has been solved analytically in several useful limiting cases and numerically over a wide range of parameters. The spurious growth rate cutoffs predicted by previous dispersion relations are absent. A novel result of this work is the dominance of inductive over electrostatic fields at high toroidal mode numbers, which stabilizes the negative-mass instability at high energies for some toroidal modes and gives a hybrid instability for others. The limited utility of a toroidal magnetic field for slowing instability growth at beam energies well above the transition energy is also noteworthy. Model predictions agree well with most available simulation data, but additional comparisons are desirable.

Several possible techniques based on inductive coupling between the beam and the accelerator cavity suggest themselves for reducing the negative-mass instability at low toroidal mode numbers and moderate to high beam energies. We

have already seen that positioning the beam near the inner wall of the torus decreases the $l = 1$ negative-mass-instability growth rate of a 10-kA beam above about 15 MeV. (That this result for a far-off-center beam carries over to beams and cavities with circular cross section remains to be proved, however.) Thin dielectric linings or weak periodic slow-wave structures in the cavity[21,22] should have similar effects but must not significantly decrease the electromagnetic cutoff frequency. Using periodic structures also creates the possibility of inducing unstable three-wave mode coupling.[13] Although reducing growth for low toroidal modes tends to increase it for high modes, beam temperature may control the latter. Implementing any of these ideas may pose serious technical problems, however. Far-off-center beams may quickly strike the wall, dielectrics outgas and flash over, and slow-wave structures are easily damaged by high-power beams. Nonetheless, additional thought given to such speculative approaches may prove fruitful.

Before concluding, we remark that other possible methods of suppressing the negative-mass instability exist. For instance, Eq. (56) predicts stability for the modified betatron when ω_r^2 and ω_z^2 are negative. The sign reversal can be accomplished by introducing trapped low-energy electrons into the accelerator,[28] or by other means which we are presently investigating.

REFERENCES

1. P. Sprangle, C. A. Kapetanakos, and S. J. Marsh, in *Proc. Fourth Intern. Conf. on High Power Electron and Ion Beams,* H. J. Doucet and J. M. Buzzi, Eds. (CNRS, France, 1981).
2. G. Barak and N. Rostoker, *Phys. Fluids* **26,** 856 (1983).
3. C. W. Robertson, A. Mondelli, and D. Chernin, *Phys. Rev. Lett.* **50,** 507 (1983).
4. S. Humphries and D. M. Woodall, *Bull. Am. Phys. Soc.* **28,** 1054 (1983).
5. D. Chernin, A. Mondelli, and C. W. Roberson, *Phys. Fluids* **27,** 2378 (1984).
6. C. A. Kapetanakos, P. Sprangle, S. J. Marsh, D. Dialetis, C. Agritellis, and A. Prakash, unpublished (1985).
7. A. Faltens, G. R. Lambertson, J. M. Peterson, and J. B. Rechen, in *Proc. IXth Intern. Conf. on High Energy Accelerators* (SLAC, Stanford, 1974).
8. R. W. Landau and V. K. Neil, *Phys. Fluids* **9,** 2412 (1966).
9. P. Sprangle and J. L. Vomvoridis, unpublished (1982).
10. B. B. Godfrey and T. P. Hughes, *Phys. Fluids* **28,** 669 (1985).
11. B. B. Godfrey and T. P. Hughes, *IEEE Trans. Nucl. Sci.* **NS-32,** 2495 (1985).
12. T. P. Hughes and B. B. Godfrey, *Appl. Phys. Lett.* **46,** 473 (1985).
13. T. P. Hughes and B. B. Godfrey, *Phys. Fluids* **29,** 1698 (1986).
14. R. Davidson and H. Uhm, *Phys. Fluids* **25,** 2089 (1982).
15. P. Sprangle and D. Chernin, *Particle Accelerators* **15,** 35 (1984).
16. T. P. Hughes, unpublished (1985).
17. P. M. Morse and H. Feshbach, *Methods of Theoretical Physics* (McGraw-Hill, New York, 1953), Part II, Chaps. 10.3 and 13.1.
18. R. E. Collin, *Can. J. Phys.* **51,** 1135 (1973).
19. M. Abramowitz and I. A. Stegun, Eds., *Handbook of Mathematical Functions* (U.S. Government Printing Office, Washington, 1964), Chaps. 9 and 11.
20. V. K. Neil and A. M. Sessler, *Rev. Sci. Instrum.* **36,** 429 (1965).
21. R. J. Briggs and V. K. Neil, *Plasma Phys.* **8,** 255 (1966).
22. R. J. Briggs and V. K. Neil, *Plasma Phys.* **9,** 209 (1967).
23. R. W. Landau, *Phys. Fluids* **11,** 205 (1968).

24. J. Walsh, B. Johnson, G. Dattoli, and A. Renieri, *Phys. Rev. Lett.* **53**, 779 (1984).
25. J. F. Traub, *Iterative Methods for the Solutions of Equations* (Prentice-Hall, Englewood Cliffs, 1964), Chap. 10.
26. C. A. Kapetanakos, P. Sprangle, D. P. Chernin, S. J. Marsh, and I. Haber, *Phys. Fluids* **26**, 1634 (1984).
27. M. M. Campbell and B. B. Godfrey, unpublished (1982).
28. G. Roberts and N. Rostoker, *Phys. Fluids* **29**, 333 (1986).

APPENDIX

Green's Function Solution to Eq. (11)

In Ref. 17, Morse and Feshbach show how to construct a Green's function for Eq. (11) in general curvilinear coordinates from solutions to the scalar Helmholtz equation. Here, we use a more direct approach, starting from the component form of the vacuum vector Helmholtz equation in cylindrical coordinates:

$$\nabla^2 E_z + \omega^2 E_z = 0, \tag{A-1}$$

$$\nabla^2 E_r - \frac{2}{r^2}\frac{\partial E_\theta}{\partial \theta} - \frac{E_r}{r^2} + \omega^2 E_r = 0,$$

$$\nabla^2 E_\theta + \frac{2}{r^2}\frac{\partial E_r}{\partial \theta} - \frac{E_\theta}{r^2} + \omega^2 E_\theta = 0.$$

Solutions are assumed to be of the form $E(r, z) \exp(il\theta - i\omega t)$. The equation for the vacuum E_z field decouples, and the eigenfunctions satisfying the appropriate boundary conditions are

$$\phi(l, k, {}^l\lambda_E) = g_E^\lambda(r) f_E^k(z), \tag{A-2}$$

where the normalized radial eigenfunction $g_E^\lambda(r)$ is given by Eq. (33), ${}^l\lambda_E$ satisfies Eq. (23), and the normalized axial eigenfunction $f_E^k(z)$ is given by

$$f_E^0 = (2a)^{-1/2} \qquad\qquad \text{for} \quad j = 0,$$

$$f_E^k = a^{-1/2}\left[\cos\frac{j\pi z}{a}, \sin\frac{(j-\frac{1}{2})\pi z}{a}\right] \quad \text{for} \quad 1 \le j < \infty. \tag{A-3}$$

Sturm–Liouville theory guarantees that the E_z eigenfunctions form a complete set, so that the Green's function for the complete solution for E_z is given by

$$G_z(l) = \sum_{k,\lambda} \frac{f_E^k(z)g_E^\lambda(r)f_E^k(z')g_E^\lambda(r')}{\omega^2 - k^2 - {}^l\lambda_E^2}. \tag{A-4}$$

The equations for E_r, E_θ are coupled, but can still be solved in terms of Bessel functions, yielding two normalized independent solutions:

$$\boldsymbol{\psi}_E(l, k, {}^l\lambda_E) = {}^l\lambda_E^{-1}f_B^k(z)\left[\frac{dg_E^\lambda(r)}{dr}\hat{\mathbf{r}} + \frac{il}{r}g_E^\lambda(r)\hat{\boldsymbol{\theta}}\right],$$

$$\boldsymbol{\psi}_B(l, k, {}^l\lambda_B) = {}^l\lambda_B^{-1}f_B^k(z)\left[-\frac{il}{r}g_B^\lambda(r)\hat{\mathbf{r}} + \frac{dg_B^\lambda(r)}{dr}\hat{\boldsymbol{\theta}}\right], \tag{A-5}$$

where g^λ_E is as in Eq. (33), g^λ_B is given by Eq. (34), $^l\lambda_B$ satisfies Eq. (24), and $f^k_B(z)$ has the form

$$f^k_B = a^{-1/2}\left[\sin\frac{j\pi z}{a}, \cos\frac{(j-\tfrac{1}{2})\pi z}{a}\right], \qquad 1 \le j < \infty. \tag{A-6}$$

ψ_E and ψ_B are orthogonal in the sense that

$$\int r\,dr\,dz\,\psi^*_E(l, k, {}^l\lambda_E)\cdot\psi_B(l, k', {}^l\lambda_B) = 0 \quad \text{for all } k, k', {}^l\lambda_E, {}^l\lambda_B, \tag{A-7}$$

where the star denotes the complex conjugate. Together, the eigenvectors in Eq. (A-5) form a complete set for the perpendicular electric field and yield the dyadic Green's function:

$$\mathbf{G}_\perp(l) = \sum_{k,\lambda}\frac{\psi_E(r, z)\psi^*_E(r', z')}{\omega^2 - k^2 - {}^l\lambda^2_E} + \frac{\psi_B(r, z)\psi^*_B(r', z')}{\omega^2 - k^2 - {}^l\lambda^2_B} \tag{A-8}$$

Applying Green's theorem to Eq. (11), we find that the solution for the electric field is given by

$$\mathbf{E} = \int \mathbf{G}\cdot(-i\omega\,\delta\mathbf{J} + \nabla\,\delta\rho)r'\,dr'\,dz', \tag{A-9}$$

where $\mathbf{G}$ stands for the total Green's function $\mathbf{G}_\perp + G_z\hat{\mathbf{z}}\hat{\mathbf{z}}'$. For example, the expression obtained for E_z is

$$E_z(r, z) = -\rho\sum_{k,\lambda}\frac{f^k_E(z)g^\lambda_E(r)}{\omega^2 - k^2 - {}^l\lambda^2_E}[(\omega\Omega - k^2)\rho^k_E\rho^\lambda_E\,\delta z + k\rho^k_B\hat{\rho}^\lambda_E\,\delta r - ilk\rho^k_B\rho^\lambda_E\,\delta\theta],$$

$$\tag{A-10}$$

where the form factors ρ^k_E, ρ^λ_E, etc., are given by Eqs. (21), (22), and (27)–(31). The magnetic fields are obtained from the electric fields by applying Faraday's Law, Eq. (12).